Distributed Flow Estimation and Closed-Loop Control of an Underwater Vehicle with a Multi-Modal Artificial Lateral Line

Levi DeVries[1], Francis D. Lagor[1], Hong Lei[2], Xiaobo Tan[2], and Derek A. Paley[1]

[1] Department of Aerospace Engineering and Institute for Systems Research, University of Maryland, College Park, MD 20742, USA

[2] Department of Electrical and Computer Engineering, Michigan State University, East Lansing, MI 48824, USA

E-mail: dpaley@umd.edu

Abstract. Bio-inspired sensing modalities enhance the ability of autonomous vehicles to characterize and respond to their environment. This paper concerns the lateral line of cartilaginous and bony fish, which is sensitive to fluid motion and allows fish to sense oncoming flow and the presence of walls or obstacles. The lateral line consists of two types of sensing modalities: canal neuromasts measure approximate pressure gradients, whereas superficial neuromasts measure local flow velocities. By employing an artificial lateral line, the performance of underwater sensing and navigation strategies is improved in dark, cluttered, or murky environments where traditional sensing modalities may be hindered. This paper presents estimation and control strategies enabling an airfoil-shaped unmanned underwater vehicle to assimilate measurements from a bio-inspired, multi-modal artificial lateral line and estimate flow properties for feedback control. We utilize potential flow theory to model the fluid flow past a foil in a uniform flow and in the presence of an upstream obstacle. We derive theoretically justified nonlinear estimation strategies to estimate the free stream flowspeed, angle of attack, and the relative position of an upstream obstacle. The feedback control strategy uses the estimated flow properties to execute bio-inspired behaviors including rheotaxis (the tendency of fish to orient upstream) and station-holding (the tendency of fish to position behind an upstream obstacle). A robotic prototype outfitted with a multi-modal artificial lateral line composed of ionic polymer metal composite (IPMC) and embedded pressure sensors experimentally demonstrates the distributed flow sensing and closed-loop control strategies.

Nomenclature

j, k	Indices
t	Time
ξ	Point in the complex plane
z	Point in the complex plane, after conformal map
x	Real part of complex number z
y	Imaginary part of complex number z; $\hat{y}$ denotes estimate of y
c_0	Conformal map parameter
R	Disk radius
ξ_0	Disk center offset
U	Free stream flowspeed
α	Angle of attack with respect to free stream flow
Γ	Circulation strength of a point vortex
W	Velocity potential function
$f(z)$	Flow velocity at location z; $f_n(z)$ denotes component of flow normal to sensor
$\boldsymbol{\Omega}$	Set of estimated flowfield parameters
d	Diameter of upstream obstacle
u_1	Cross-stream velocity control input
u_2	Angular velocity control input
N_p	Number of pressure sensors
N_f	Number of velocity sensors
$P(z)$	Pressure at location z
ρ	Fluid density
$\boldsymbol{\beta}$	Set of measurements; $\tilde{\boldsymbol{\beta}}$ denotes measurements corrupted by noise
ΔP_{ij}	Pressure difference between sensors i and j
$\boldsymbol{q}(\cdot)$	Multi-modal measurement function
η	Zero-mean Gaussian noise
σ^2	Variance of Gaussian noise
$\boldsymbol{A}$	Set of observations from all sensors
$p(\cdot)$	Probability density function
Ψ	Linear motion matrix
Σ_p	Process noise
χ	Standard deviation of a set of IPMC measurements
a_k, b_k	Calibration coefficients of the kth IPMC sensor
K	Control gain

1. Introduction

Biologically inspired sensing modalities enable autonomous underwater vehicles to navigate unknown, murky, and cluttered environments that challenge traditional sensing

technologies [1]. For example, the lateral line of cartilaginous and bony fish and some aquatic amphibians [2],[3] is sensitive to fluid motion around the fish's body and provides a data source for flowfield estimation. Engineered systems that emulate the sensing abilities of the lateral line may enable autonomous or remote operation of underwater vehicles even when sensing strategies such as sonar or vision are inhibited. This paper presents theoretical and experimental results demonstrating the design and implementation of an artificial lateral line to estimate properties of a flowfield and the use of these estimated properties in real-time for feedback control of an unmanned underwater vehicle.

Stream-dwelling fish have a remarkable ability to navigate tumultuous, unknown environments riddled with obstacles [4]. In fact, many species exhibit a behavior known as station-holding, in which individuals are able to sense the relative position of an obstacle in a current and hold position in its wake [1]. Similarly, fish are known to orient upstream in a flowfield, a behavior known as (positive) rheotaxis [4]. These behaviors are mediated by sensing modalities such as vision and the lateral line. In fact, fish are able to navigate in the absence of light or without vision [4]. The lateral line is also believed to play an important role in schooling [5] and sensing predators [6], prey [7], and other features in the environment [8],[9]. This paper presents sensing and control algorithms using an artificial lateral line to enable autonomous execution of rheotaxis and station-holding, which serve as basic motion primitives for underwater vehicle missions.

The lateral line system is composed of hundreds to thousands of receptors, known as neuromasts, distributed along the body of the fish [1]. Neuromasts are divided into two categories. Superficial neuromasts, which are located on the external surface of the fish, consist of hair cells encased in a gelatinous dome called a cupula [3] and sense local flow velocity [10]. Canal neuromasts are located under the skin in fluid filled canals and sense pressure differences between adjacent pores of the canal [11].

Recent works describe an artificial lateral line for underwater vehicle sensing with a single modality only [12],[13]. For example, Yang *et al.* [12] created artificial superficial neuromasts using an array of micro-fabricated hot-wire anemometry sensors. Artificial superficial neuromast sensors have also been developed using ionic polymer metal composites (IPMC) [14] and multi-layered silicon beams [15]. (For a comprehensive review of biomimetic hair sensors similar to the superficial neuromast system, see Tao and Yu [13].) Other works have emulated the function of canal neuromasts using pressure [11],[16],[17], optical [18], and capacitive [19] sensor arrays. This paper presents the first known use of a multi-modal artificial lateral line with both pressure-difference and local velocity sensors. Using a multi-modal lateral line increases system robustness to individual sensor failure and the observability of flow properties that are only weakly detectable by one modality or the other. As we show, an additional benefit of using both pressure-difference and velocity sensing is the ability to greatly simplify sensor calibration using a novel bootstrapping procedure.

Several previous works have implemented unimodal sensor arrays for bio-inspired

flow sensing and closed-loop control. Gao and Triantafyllou [20] used a pressure sensor array to control the angle of attack of an underwater vehicle with respect to a free stream flow. Salumae and Kruusma used pressure-difference measurements to demonstrate rheotaxis [21]. In other work, the same authors used heuristic methods to demonstrate station-holding [22]. Fernandez used particle filtering techniques to track vortices near a pressure sensor array [23], whereas Venturelli *et al.* [11] showed that the position of a Karman vortex street can be discriminated using a pressure sensor array.

This paper presents flow sensing and control strategies to provide model-based feedback control algorithms enabling an underwater vehicle to autonomously emulate bio-inspired behavior. We use a multi-modal artificial lateral line equipped with both pressure and velocity sensor arrays. The technical approach is to utilize tools from potential flow theory and nonlinear estimation and control to model the flow around a streamlined foil. Nonlinear estimators assimilate noisy measurements to estimate quantities of interest in the flowfield and feedback controllers replicate the desired behavior. We implement the estimation and control strategies on a $\sim$10 cm robotic testbed equipped with a multi-modal artificial lateral line and estimate flowspeed and angle of attack of the flowfield in a laboratory-scale flow channel. A key aspect of the control testbed is that the measurements are integrated by the nonlinear estimator over space and time to overcome model error and to resolve uncertain features of the flow environment such as the size and relative position of an upstream obstacle.

The contributions of this work are (1) the design of distributed estimation algorithms that allow an underwater vehicle to estimate properties of an underwater environment by assimilating noisy measurements from pressure and velocity sensors; (2) closed-loop control algorithms incorporating estimated flowfield properties to enable an underwater vehicle to emulate rheotaxis and station-holding behaviors; and (3) experimental demonstration of the bio-inspired estimation and control techniques using an artificial lateral line composed of ionic polymer metal composite (IPMC) and embedded pressure sensors. To incorporate both sensing modalities, we present a novel bootstrapping calibration strategy that leverages the strengths of pressure sensing in order to associate IPMC sensor amperage measurements with local flow velocity.

The paper proceeds as follows. Section 2 uses potential flow theory to model the flow around a streamlined underwater vehicle in a uniform flowfield and in the wake of an obstacle. Section 3 presents a state-space motion and measurement model for an underwater vehicle outfitted with a multi-modal artificial lateral line and derives nonlinear estimation strategies allowing an underwater vehicle to estimate the flowfield. Section 4 presents the design, fabrication, and implementation of a bio-inspired lateral line incorporating IPMC and pressure sensors in distributed arrays. It also presents a novel bootstrapping method enabling calibration of the multi-modal artificial lateral line without external flow or orientation references. Section 5 presents experimental results demonstrating rheotaxis and station-holding behaviors using the artificial lateral line control system. Section 6 summarizes the paper and ongoing work.

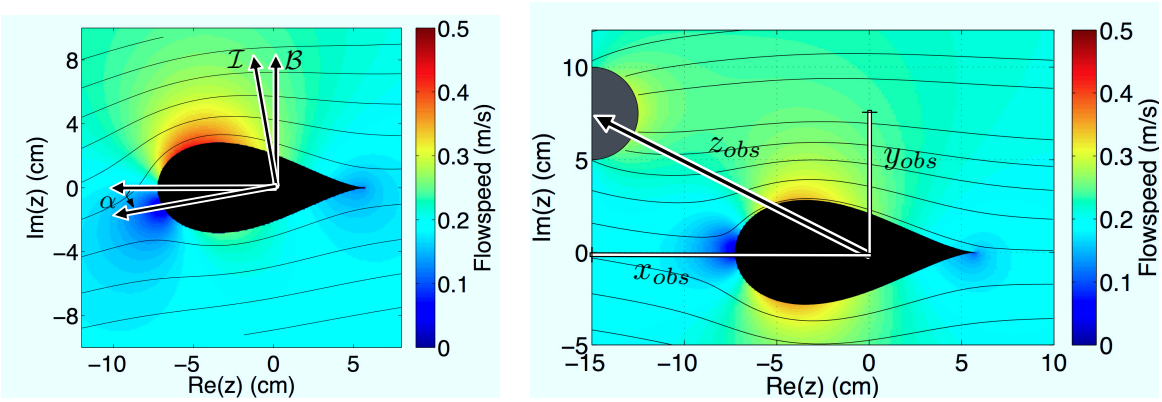

(a) (b)

Figure 1. Simulated uniform flowfield with free stream flowspeed $U = 0.2$ m/s around (a) a foil with $(R, \xi_0) = (4.35, -1.5)$ cm at angle of attack $\alpha = 10°$ and (b) a foil in the wake of a 5 cm diameter cylinder and angle of attack $\alpha = 0°$.

2. Fluid and Vehicle Modeling

This section describes a two-dimensional model of fluid flow past a streamlined foil. We use elementary potential flow functions to first model the flow around a disk in the complex plane, which is then transformed to produce the flow around a foil using conformal mapping [24]. The flow models developed in this section are used in Sections 3 and 5 to design and implement estimation and control strategies for bio-inspired behavior. Section 2.1 describes a model of a foil in the presence of a uniform flowfield without obstacles. Section 2.2 augments the uniform flow model by including an upstream bluff body at moderate to high Reynolds numbers, in which the obstacle produces a turbulent wake [23]. The analytical flow models developed in this section approximately capture the general flow structure and are implemented in Section 3 to facilitate realtime estimation of flowspeed and angle of attack and—if present—the size and relative position of an upstream obstacle.

2.1. Obstacle-free Flow Model

Consider a point $\xi \in \mathbb{C}$ in the complex plane. The coordinate transformation [24]

$$z = \xi + \frac{c_0^2}{\xi} \in \mathbb{C}, \tag{1}$$

maps shapes according to the transformation variable $c_0 \in \mathbb{R}$. In particular, choosing $c_0 = R - |\xi_0|$ maps a disk of radius R offset along the real axis by $\xi_0 \in \mathbb{R}$ to a symmetric, streamlined foil as shown in Figure 1(a) [24]. Note, the foil shape is defined by the transformation (1) and the parameters (R, ξ_0).

Using the mapping (1), we model the flow around a disk in the complex plane in order to generate the corresponding flow around a foil. Assuming an inviscid, incompressible and irrotational fluid (which is justified at low flow speeds where flow separation and viscous effects are minimal [24]), the flow around a disk is represented

by the sum of elementary potential functions. Let $U > 0$ be the free stream speed of the uniform flow, α denote the angle of attack of the foil relative to the free stream flow, and $\Gamma_{disk} \in \mathbb{R}$ denote the circulation of a vortex. (Note the potential flow approximation is valid only for small angles of attack, so we take $\alpha \in [-15°, 15°]$ to be consistent with symmetric foils at low Reynolds numbers [25].) The velocity potential is [24],[26]

$$W_{uni}(\xi) = U(\xi - \xi_0)e^{-i\alpha} + \frac{R^2}{\xi - \xi_0} U e^{i\alpha} - \frac{i\Gamma_{disk}}{2\pi} \ln(\xi - \xi_0). \tag{2}$$

The terms on the right-hand side correspond to the uniform flow, a doublet, and a vortex located at the center of the disk [24],[26]. The final term on the right-hand side of (2) represents the potential due to a vortex centered at ξ_0 that enforces flow stagnation at the trailing edge of the foil [24].

For any velocity potential function, the conjugate flow $f^* = u - iv$ is the gradient of the potential taken with respect to z-coordinates, i.e., [24]

$$f^*(z) = \frac{\partial W}{\partial \xi} \left(\frac{\partial z}{\partial \xi} \right)^{-1}. \tag{3}$$

For any velocity potential corresponding to flow around the foil, the Kutta condition [24],[26] stipulates that the flow must be continuous around the foil, which implies that the flow must stagnate at the foil's trailing edge. This condition determines the vortex circulation Γ_{disk} in (2) by enforcing $f^*(z) = 0$ in (3) at the foil's trailing edge, giving $\Gamma_{\text{disk}} = -4\pi RU \sin\alpha$ [24],[26]. For a known body shape (R, ξ_0), the uniform flowfield (3) is parameterized by the set‡ $\mathbf{\Omega}_{uni} = (U, \alpha)$ characterized by the free stream flowspeed and angle of attack. Equation (3) with velocity potential (2) generates the streamlines and flowspeed illustrated in Figure 1(a).

Note that (3) provides the flow around the foil in ξ-plane coordinates rather than in z coordinates. The inverse of the Joukowski mapping (1) yields the z-plane coordinates [9]. We concern ourselves only with points outside the disk to calculate the conjugate flow f^*, as shown in Figure 1(a). The figure also shows how we measure the angle of attack α of the body-fixed reference frame $\mathcal{B}$ attached to the foil relative to the lab-fixed reference frame $\mathcal{I}$ aligned with the upstream direction.

2.2. Modeling an Obstacle at Moderate to High Reynolds Number

This section augments the uniform flow model by including the wake behind an obstacle. At relatively high flow speeds (equivalently Reynolds numbers) the wake becomes turbulent and is characterized by an envelope of turbulent flow downstream of the obstacle [23]. The flowfield is a solution to the two-dimensional Navier-Stokes equation, which can not be solved in real time but often admits simplified approximations [27]. Many authors have used potential theory to approximate the obstacle wake structure by including a combination of elementary potential functions such as sources and sinks [28],[29]. To maintain computational simplicity in the model used for real-time

‡ We use bold fonts to represent a column matrix, e.g., of sensor positions $\mathbf{z} = [z_1\ z_2\ ...\ z_N]^T$, or a set of parameters, e.g., $\mathbf{\Omega} = (\Omega_1, \Omega_2, \ldots, \Omega_M)$.

estimation, we approximate the flow by modeling the obstacle and its associated wake as a point source located at the center of the true obstacle position. Although the potential flow model introduces model error compared to the real flow conditions, it nonetheless sufficiently describes the general wake structure [23].

Let $z_{obs} = x_{obs} + iy_{obs}$ denote the position of the obstacle in the z-plane, where x_{obs} is the upstream component and y_{obs} denotes the cross-stream component relative to the foil (at $\alpha = 0$) [23]. This method generates an obstacle commonly referred to as a Rankine half body [26],[23]. The inverse of the Joukowski mapping (1) gives the obstacle position relative to the cylinder in ξ coordinates, denoted by ξ_{obs}. Let d be the obstacle diameter. Augmenting the uniform flow potential (2) with the point source and using using the Milne-Thomson Circle Theorem [30] to ensure no normal flow through the surface of the disk gives the obstacle potential function

$$W_{obs}(\xi) \;=\; W_{uni} + \tfrac{d}{2}\ln(\xi - \xi_{obs}) + \tfrac{d}{2}\ln(\tfrac{R^2}{\xi} - \xi^*_{obs}). \tag{4}$$

Equation (3) with velocity potential (4) provides the conjugate flow relative to the foil. Note that the wake model is characterized by four parameters, i.e., $\mathbf{\Omega}_{obs} = (U, \alpha, z_{obs}, d)$. Figure 1(b) illustrates the flowfield model (4) for a cylindrical obstacle with diameter $d = 5$ cm. The obstacle is superimposed over the source location and its position $z_{obs} = x_{obs} + iy_{obs}$ relative to the foil is shown. Note the streamlines curve outward around the obstacle surface.

3. State-Space Modeling and Estimation

3.1. Motion and Measurement Model

As described in Section 4, the foil is connected to a robotic gantry system capable of kinematic control of its cross-stream position y and orientation α relative to the oncoming flow. Under the kinematic-control assumption we have

$$\begin{aligned} \dot{y} &= u_1 \\ \dot{\alpha} &= u_2, \end{aligned} \tag{5}$$

where u_1 and u_2 are the cross-stream velocity and rotation-rate control inputs, respectively.

The foil is outfitted with N_f flow sensors located at positions $z_{f_i} \in \mathbb{C}$, $i = 1, \ldots, N_f$ with sensor length l and N_p pressure sensors located at positions z_{p_j}, $j = 1, \ldots, N_p$. The flow velocity at each sensor position is given by the conjugate of the flow model (3) or (4) evaluated at the sensor location. Assume that the ith velocity sensor measures the square of the component of the flow normal to the sensor orientation at the tip of the sensor, denoted $|f_n(z_{f_i})|^2$. Each pressure sensor measures the local pressure given by Bernoulli's equation [26]

$$P(z_{p_j}; \mathbf{\Omega}) = C - \tfrac{1}{2}\rho |f(z_{p_j}; \mathbf{\Omega})|^2, \tag{6}$$

where ρ is the density of water and C is a constant. To eliminate dependence on the constant C we use the difference in pressure between two measurement locations

$\Delta P_{i,j} = P(z_{p_i};\mathbf{\Omega}) - P(z_{p_j};\mathbf{\Omega})$, analogous to the canal neuromast architecture in fish. The equations representing measurements from N_f flow sensors and N_m pressure difference measurements are

$$\begin{aligned} \beta_1 &= |f_n(z_{f_1};\mathbf{\Omega})|^2 \\ &\vdots \\ \beta_{N_f} &= |f_n(z_{f_{N_f}};\mathbf{\Omega})|^2 \\ \beta_{N_f+1} &= \Delta P_{1,2} \\ &\vdots \\ \beta_{N_f+N_m} &= \Delta P_{N_p-1,N_p}, \end{aligned} \tag{7}$$

where $N_m = \frac{N_p!}{2!(N_p-2)!}$ is the number of unique pressure-sensor pairs. Let $\boldsymbol{z} = \begin{bmatrix} z_1 \dots z_{N_f+N_p} \end{bmatrix}^T$ and $\boldsymbol{\beta} = \begin{bmatrix} \beta_1 \dots \beta_{N_f+N_m} \end{bmatrix}^T$ be $N_i \times 1$ vectors of the measurement positions and flow measurements, respectively.

Combining the motion model (5) with the measurement model (7) under the assumption that the vehicle moves quasi-statically in a uniform flow (3) gives the nonlinear state-space model

$$\begin{aligned} \dot{y} &= u_1 \\ \dot{\alpha} &= u_2 \\ \boldsymbol{\beta} &= \boldsymbol{q}(\boldsymbol{z};\mathbf{\Omega}_{uni}), \end{aligned} \tag{8}$$

where $\boldsymbol{q}(\cdot) \in \mathbb{R}^{(N_f+N_m)\times 1}$ represents the measurement function in (7). For a known body shape (R, ξ_0), the uniform flowfield (3) is parameterized by the two-dimensional parameter space $\mathbf{\Omega}_{uni} = (U, \alpha)$. By assimilating measurements collected at the sensor locations $\boldsymbol{z}$, one can reconstruct the flowfield by estimating $\mathbf{\Omega}_{uni}$.

In the presence of an upstream obstacle, the flow is modeled by (4). We write the kinematics of the obstacle relative to the body-fixed reference frame $\mathcal{B}$, where for simplicity we assume the angle of attack is held fixed at zero for all time. This yields the state-space model of an obstacle at moderate to high Reynolds number

$$\begin{aligned} \dot{y}_{obs} &= -u_1 \\ \boldsymbol{\beta} &= \boldsymbol{q}(\boldsymbol{z};\mathbf{\Omega}_{obs}). \end{aligned} \tag{9}$$

Note, optimization of the positions of pressure and flow velocity sensors in order to maximize flowfield observability is outside the scope of this paper and has been partially addressed elsewhere [10],[31].

3.2. Flowfield Estimation

This section presents a recursive Bayesian filtering algorithm to estimate an unknown flowfield using a sensor array. Due to its simplicity of implementation, the grid-based recursive filter is advantageous for low-dimensional state-space representations of the flowfield with linear parameter kinematics and nonlinear measurement models such as the flow models (3) and (4).

Estimation of a spatiotemporal flowfield of the form (3) can be accomplished by assimilating noisy measurements. For linear systems with Gaussian noise the optimal Bayesian filter is the Kalman filter, whereas for nonlinear systems with nonlinear noise models a common Bayesian filter is a particle filter [32]. In either case, the flow estimate is encapsulated in a state vector, which for example may contain the flow velocity at a large number of grid points. An alternative we pursue here is a state $\mathbf{\Omega}$ that contains only a set of parameters from which the flowfield can be reconstructed. This representation provides a significant reduction in computations, making it attractive for use in a dynamic feedback controller. (Note that this representation is only possible for a parameterized flowfield.) For example, the uniform flow model (3) is defined by the parameters $\mathbf{\Omega}_{uni} = (U, \alpha)$, such that the flowfield at z_k is $f_k = u(z_k; \mathbf{\Omega}) + iv(z_k; \mathbf{\Omega})$, whereas the obstacle flow (4) is parameterized by $\mathbf{\Omega}_{obs} = (U, \alpha, z_{obs}, d)$.

The Bayesian formalism proceeds as follows [32]. Let $\hat{\mathbf{\Omega}}$ denote the parameter estimates and $\tilde{\beta}_k = \beta_k + \eta_k$ denote a noisy observation collected from the k^{th} sensor (or sensor pair), where we assume the noise η_k is normally distributed with zero mean and variance σ_k^2. Denote $\mathbf{A} = \{\tilde{\beta}_1, \ldots, \tilde{\beta}_{N_f+N_m}\}$ as the set of observations from all sensors. The posterior probability of the state $\mathbf{\Omega}$ given the measurements $\mathbf{A}$ is

$$p(\mathbf{\Omega}|\mathbf{A}) = \kappa p(\boldsymbol{A}|\mathbf{\Omega}) p(\mathbf{\Omega}|\mathbf{A}_0), \tag{10}$$

where κ ensures that $p(\mathbf{\Omega}|\mathbf{A})$ has unit integral over the state space. The likelihood function $p(\mathbf{A}|\mathbf{\Omega})$ represents the conditional probability of the observations $\mathbf{A}$ given the state $\mathbf{\Omega}$ and $p(\mathbf{\Omega}|\mathbf{A}_0)$ represents the prior probability distribution. Note that, in the absence of observations or any information other than parameter bounds, the prior probability $p(\mathbf{\Omega}|\mathbf{A}_0)$ is uniform.

For each point $\mathbf{\Omega}$ in the state space, we choose a multivariate Gaussian likelihood function for the flow measurements $\tilde{\beta}_k$, $k = 1, \ldots, N_f$,

$$p(\tilde{\beta}_k|\mathbf{\Omega}) = \tfrac{1}{\sqrt{2\pi}\sigma_{f_k}} \exp\left[-\tfrac{1}{2\sigma_{f_k}^2}\left(|f_n(z_{f_k}; \mathbf{\Omega})|^2 - \tilde{\beta}_k\right)^2\right], \tag{11}$$

and for the pressure difference measurements $\tilde{\beta}_j$, j=N_f+1, $\ldots$, $N_f + N_m$,

$$p(\tilde{\beta}_j|\mathbf{\Omega}) = \tfrac{1}{\sqrt{2\pi}\sigma_{p_j}} \exp\left[-\tfrac{1}{2\sigma_{p_j}^2}\left(\Delta P_j(\mathbf{\Omega}) - \tilde{\beta}_j\right)^2\right], \tag{12}$$

respectively. Choosing Gaussian likelihood functions in (11) and (12) ensures that measurements equal to the theoretically predicted values are assigned the largest probability density, although the Gaussian form is not required for this method. Assuming that the measurements are taken from $N_f + N_m$ sensors, the posterior probability density of the parameter estimate $\mathbf{\Omega}$ is obtained using the joint measurement likelihood combining both flow and pressure difference measurements as follows:

$$p(\mathbf{\Omega}|\mathbf{A}) = \kappa \left(\prod_{k=1}^{N_f+N_m} p(\tilde{\beta}_k|\mathbf{\Omega})\right) p(\mathbf{\Omega}|\mathbf{A}_0), \tag{13}$$

where $p(\tilde{\beta}_k|\mathbf{\Omega})$ is given by (11) for $k = 1, \ldots, N_f$ and (12) for $k = N_f + 1, \ldots, N_f + N_m$. The point $\hat{\mathbf{\Omega}}$ in the parameter space corresponding to the maximum (mode) of the

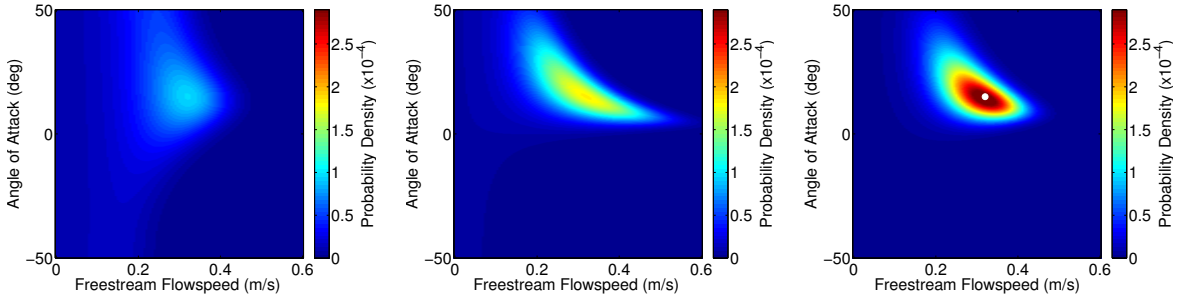

Figure 2. Assimilation of spatially distributed velocity and pressure-difference measurements. (a) Likelihood function from eight flow sensor measurements; (b) likelihood function from six pressure-difference measurements; and (c) the resulting posterior probability density. The ground truth parameter values are illustrated by the white circle.

posterior probability $p(\mathbf{\Omega}|\mathbf{A})$ provides the maximum likelihood estimate of the flowfield parameters.

Figure 2 illustrates the likelihood and posterior probability density functions corresponding to assimilation of flowspeed and pressure difference measurements at one time instant, assuming the uniform flow model (2) is used to estimate the free stream parameters $\mathbf{\Omega}_{uni} = (0.3 \text{ m/s}, 10^\circ)$. Figure 2(a) shows the likelihood function resulting from assimilating eight flow sensor measurements, starting from a uniform prior distribution where $\sigma_{f_k} = 0.01$ m/s for sensors $k = 1, \ldots, 8$. Figure 2(b) illustrates the likelihood function resulting from assimilation of six pressure difference measurements (from four pressure sensors), where $\sigma_{p_j} = 0.2$ KPa for all $j = 1, \ldots, 6$ pressure differences.

A key benefit of the Bayesian approach is its ability to fuse data from multiple noisy sensing modalities. Figure 2(c) shows the posterior probability density resulting from combined pressure and flow velocity sensing. The white circle corresponds to the true flowfield parameters. Note in Figures 2(a) and 2(b) that the flow velocity and pressure difference measurements are complementary in the following sense. At this angle of attack, the flow velocity measurements tend to reduce uncertainty in the flowspeed, whereas the pressure difference measurements tend to reduce uncertainty in the angle of attack. Fusing the two modalities results in a tighter probability density around the true flowfield parameters than would be obtained from either one alone.

Equation (13) represents spatial integration over the sensor array. Temporal integration is accomplished in the Bayesian framework by using the posterior at time step $t-\Delta t$ to generate the prior at time t, i.e.

$$\begin{aligned} p(\mathbf{\Omega}(t)|\overline{\mathbf{A}}(t)) \;\; = \;\; & \kappa\Big(\textstyle\prod_{k=1}^{N} p(\tilde{\beta}_k(t)|\mathbf{\Omega}(t))\Big) \int p(\mathbf{\Omega}(t)|\mathbf{\Omega}(t{-}\Delta t)) \\ & p(\mathbf{\Omega}(t{-}\Delta t)|\overline{\mathbf{A}}(t{-}\Delta t))\mathrm{d}\mathbf{\Omega}(t-\Delta t), \end{aligned} \tag{14}$$

where $\overline{\mathbf{A}}(t) = \{\mathbf{A}(t), \mathbf{A}(t-\Delta t), \ldots, \mathbf{A}(0)\}$ represents all measurements up to time t and the motion model $p(\mathbf{\Omega}(t)|\mathbf{\Omega}(t{-}\Delta t))$ updates the probability density function from

$t - \Delta t$ to t [33, p.372-375]. Define the motion matrix Ψ and let $p(\mathbf{\Omega}(t)|\mathbf{\Omega}(t-\Delta t)) = \mathcal{N}(\Psi\mathbf{\Omega}(t-\Delta t); \Sigma_p)$, where $\mathcal{N}(\Psi\mathbf{\Omega}(t-\Delta t); \Sigma_p)$ is normally distributed white noise with mean $\Psi\mathbf{\Omega}(t-\Delta t)$ and variance Σ_p.

The recursive Bayesian filter is used in Section 5 to estimate the flow parameters relevant for the design of rheotactic and station-holding controllers. For rheotaxis, the state-space of the recursive Bayesian filter is two-dimensional and corresponds to the free stream flow parameters $\mathbf{\Omega}_{uni} = (U, \alpha)$. For station holding in moderate to high Reynolds number, we utilize the recursive Bayesian filter to estimate a subset of the parameters defining the wake model (4) such that the filter state-space corresponds to the cross-stream position of the obstacle and the obstacle diameter $\mathbf{\Omega}_{obs} = (y_{obs}, d)$.

4. Experimental Testbed for Flow Sensing and Control

This section describes the experimental hardware and software architecture implemented to demonstrate bio-inspired flow sensing and control. Section 4.1 presents the design and fabrication of the submerged foil. Section 4.2 describes the flow tank hardware and gantry system for controlling the foil motion. Section 4.3 presents experimental data confirming that the IPMC sensors are sensitive to the square of the component of the flow normal to the sensor at its location. Section 4.4 presents a novel bootstrapping strategy that employs the pressure sensors to calibrate the IPMC sensors at multiple angles of attack and flow speeds.

4.1. IPMC Flow Sensors

Ionic polymer-metal composites are an important class of electroactive polymers with built-in actuation and sensing capabilities [34],[35]. IPMCs have inherent sensing properties: an applied force or deformation on an IPMC beam yields a detectable electrical signal (typically open-circuit voltage or short-circuit current) across the electrodes [36]. The direct mechanosensory property and inherent polarity of IPMCs are essential to the construction of an artificial lateral line system and the collection of flow information. (For a detailed discussion of the mechanosensory and manufacturing process of IPMC sensors the interested reader is referred to [14] and [37].)

We designed and constructed a robotic fish prototype outfitted with eight IPMC sensors and four embedded pressure sensors [38],[36]. The robot prototype is a 3D-printed 2D-airfoil shape characterized by Joukowski mapping parameters $(R, \xi_0, c_0) = (4.35, -1.5, 2.85)$ cm and extruded in the vertical direction, as shown in Figure 3. The prototype is designed using a modular approach to (1) enable convenient installation and replacement of both IPMC and pressure sensors, (2) maintain flexibility in the number and placement of sensors around the foil, and (3) ensure a compact structure appropriate for its operating environment. The body has ten clamping blocks on each side, providing twenty sensor mounting slots for IPMC sensors, as shown in Figure 3(b). Above the IPMC sensor blocks, the foil has nine slots for mounting the pressure sensors,

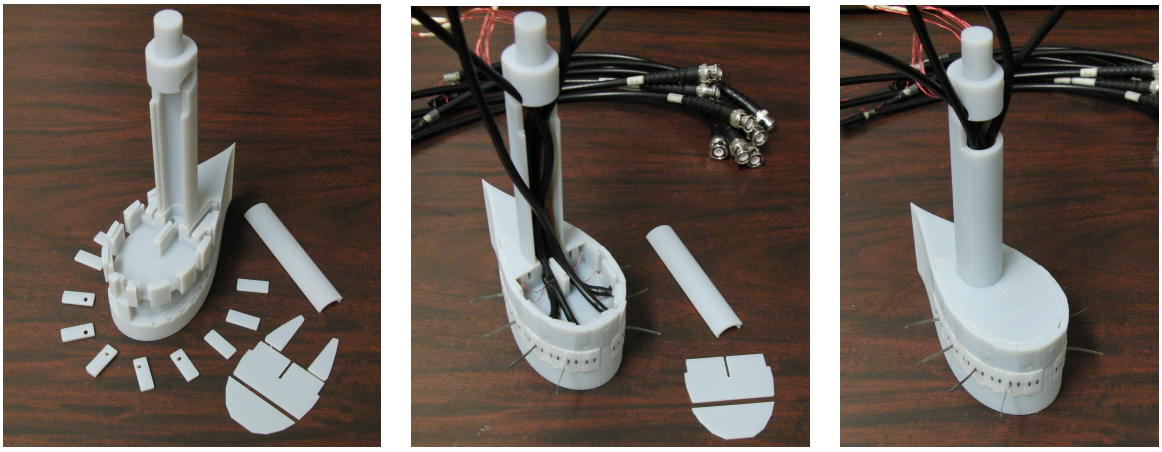

(a) (b) (c)

Figure 3. Modular design of robotic foil. An array of eight IPMC sensors are installed below an array of four pressure sensors.

as shown in Figure 3(a). We mount the pressure sensors above the IPMC sensor block to minimize fluid effects created by the IPMC sensors, which protrude into the flow. There are four pairs of symmetric slots for pressure sensors and an additional slot at the nose of the body. We use four Millar Instruments (SPR-524) Mikro-Tip Catheter Pressure Transducers encased in an open ended Delrin sheath using Teflon tape. The sensors are mounted in the forward-most symmetric slots, as shown in Figure 3(b) [10]. Mounted in this fashion, the pressure sensors measure the static pressure, which enables analysis using the potential flow model in Section 2. The extra slots allow flexibility in the sensor configuration and provide the opportunity to expand the sensor array for future experiments. This compact design maintains the smooth surface of the foil while providing enough clamping force to hold all the sensors, as shown in Figure 3(c).

4.2. Instrumentation, Control Software, and Flowfield Generation

Eight IPMC sensors are placed uniformly around the front and sides of the prototype, subject to manufacturing design constraints. The polar angles of the sensors are $\pm 84.9°$, $\pm 105.6°$, $\pm 130.7°$, and $\pm 161.0°$, measured with respect to the origin as defined in Section 2.1. The sensor length direction is normal to the foil surface and each sensor is mounted such that it responds to the two-dimensional flow (z-plane) tangential to the foil surface at the mount point. Similarly, the polar angles of the four pressure sensors are $\pm 156.3°$ and $\pm 170.7°$, respectively. Amplified sensor measurements are assimilated into the recursive Bayesian filter by incorporating Matlab functionality within a LabVIEW software interface.

We generate a uniform flowfield using a 185 L flow tank with an enclosed test section measuring $25 \times 25 \times 87.5$ cm. The vehicle's orientation and cross-stream position are controlled using an overhead gantry system, elevated using a custom made 80/20 support structure. The interested reader is referred to [10] for an extensive discussion

of the gantry and flow generation apparatus used in this work.

4.3. IPMC Flow Sensor Analysis

IPMC sensors produce measurements whose magnitudes are proportional to the amplitude of vibration, which motivates the need to better understand basic components of the flow captured by each IPMC sensor measurement. The structural and electro-mechanical modeling of an IPMC sensor subjected to pressure distributions created by a moving fluid remains the subject of ongoing work. This section presents experimental results suggesting that the standard deviation of the magnitude of each IPMC measurement corresponds closely to the component of the flow normal to the sensor, evaluated at its tip. This finding confirms that the IPMC sensors reflects local flowspeed information, emulating the superficial neuromast system of the fish lateral line [3].

By collecting data at varying angles of attack and flow speeds, we find a strong correlation between the amplitude of the AC signal measured by each sensor and the square of the component of flow velocity normal to the sensor evaluated at the sensor tip, as generated using the potential flow model (2). Figure 4(a) shows the result of fitting the standard deviation, denoted $\chi(z_{f_k}; \mathbf{\Omega}_{uni})$, of measurements collected by the sensor with polar angle 130.7° ($k = 3$) for twenty seconds at flow speeds $U \in [0, 0.6]$ m/s and angles from $\alpha = -35°$ to $\alpha = 35°$ (gray surface) to the potential flow model (red surface). Fitted data are collected for 20 seconds at 500 Hz for each flowspeed and angle of attack combination. The standard deviation $\chi(z_k; \mathbf{\Omega}_{uni})$ of each 20 second data collection at $M = 150$ different flowspeed and angle of attack combinations was calculated to generate the gray surface shown in Figure 4(a).

The flowfield estimation algorithm requires a mapping between the sensor measurements (in μA) and the potential flow measured at the sensor location (in m/s). To accomplish this mapping we compute optimal fitting coefficients (a_k, b_k) to the potential model by minimizing the mean absolute error fitting metric

$$J_k = \frac{1}{M} \sum_{j=1}^{M} \left\| (a_k \chi_j(z_k; U_j, \alpha_j) + b_k) - |f_n(z_k; U_j, \alpha_j)|^2 \right\|, \tag{15}$$

for sensors $k = 1, \ldots, 8$ and flow condition combinations $j = 1, \ldots, M$. The gray surface in Figure 4(a) shows the fitted standard deviation measurements corresponding to the sensor with polar angle 130.7° (sensor 3). The mean absolute error in each sensor and the total mean absolute error§ over all flow speeds, angles of attack, and sensors are shown in Figure 4(b).

Although Figure 4(a) shows one of the poorest model fits, out of all sensors, the general structure follows the trend of the potential flow model. Also note that the areas

§ We use the term *mean absolute error* to refer to the error of a single sensor over all flow conditions, whereas the *total mean absolute error* denotes the mean absolute error over all sensors in the array and all flow conditions.

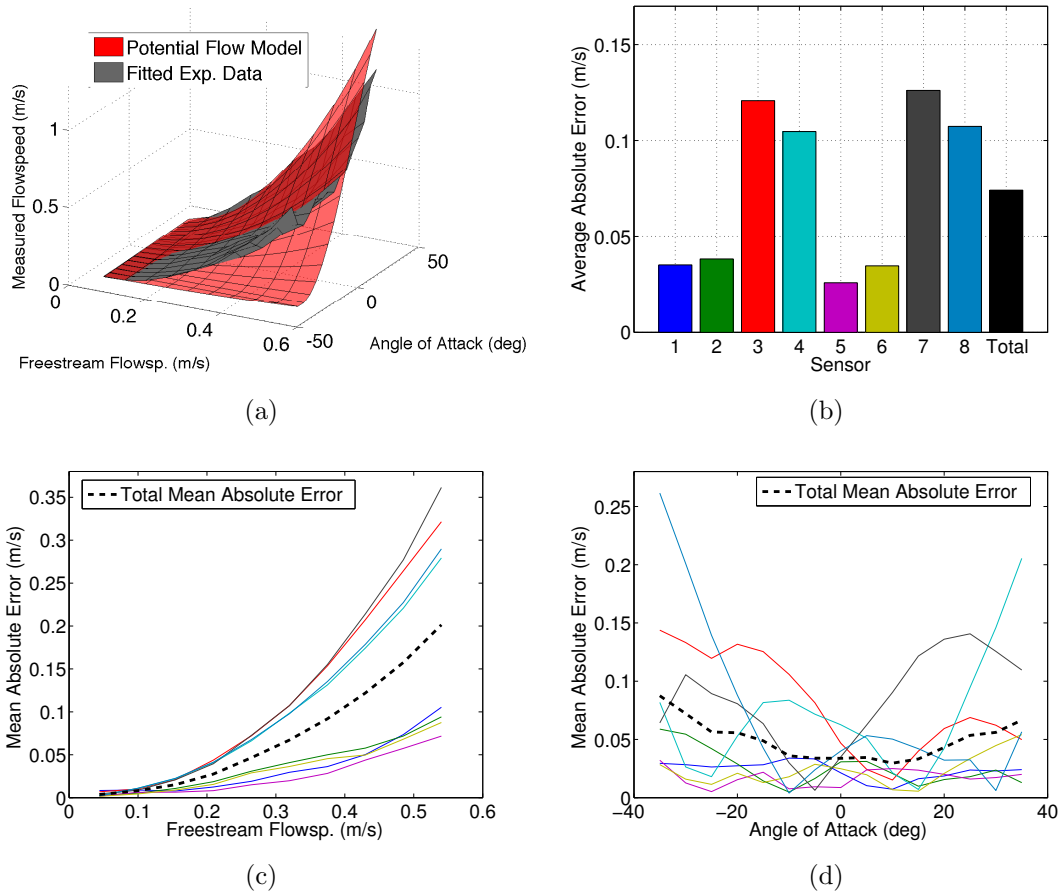

Figure 4. (a) Result of fitting the standard deviation of IPMC measurements (gray) to the component of flow normal to the sensor located at polar angle 130.7° (red). (b) Mean absolute error in fit for each sensor. (c) Mean absolute error plotted versus flowspeed; the dashed black line represents the total mean error over all sensors. (d) Mean absolute error plotted versus angle of attack. The color of each line in (c) and (d) corresponds to the sensor in (b). Note that unmodeled fluid effects increase the mean absolute error with flowspeed and angle of attack.

of the flowspace (U, α) corresponding to the largest disagreement between the measured and theoretical data lie at higher flowspeeds and angles of attack where unmodeled flow separation and viscous effects are likely. This effect is illustrated in Figures 4(c) and 4(d), which show the mean absolute error and total mean absolute error plotted versus the free stream flowspeed and angle of attack, respectively. The total mean absolute error is defined as the mean of the absolute error over all IPMC sensors in the array and is illustrated by the dashed black line in each figure. Based on Figures 4(c) and 4(d), measurement model error is proportional to flowspeed and angle of attack, implying that one can expect estimation performance to increase with decreasing flowspeed and angle of attack.

4.4. Bootstrapping the IPMC Sensors

An important benefit of the multi-modal artificial lateral line is its ability to leverage the use of one sensing modality (pressure differences) to calibrate another modality (IPMC sensors). This section presents a novel calibration procedure that utilizes the pressure sensor array to calibrate the IPMC sensor array without external flow or orientation references. Computing the calibration coefficients for each IPMC sensor as described in the previous section requires external references of the angle of attack and flowspeed. Prior work has shown that assimilating pressure difference measurements provides accurate estimation of flowspeed but often incorrectly estimates the angle of attack [10]. By zeroing out pressure differences [10],[11] using a sequence of non-symmetric sensor pairs, the vehicle steers to fixed angles of attack relative to the free stream flow velocity. Using pressure-difference measurements to estimate the flowspeed, the calibration procedure is completed without prior knowledge of the flow condition or external reference for angle of attack.

The procedure leverages the ability of pressure sensors to provide accurate estimation of the free stream flowspeed and utilizes pressure-differencing control to steer the vehicle to orientations with zero pressure difference, as illustrated in Figure 5. We use a proportional feedback controller based on the pressure difference $\Delta P_{ij} = P(z_{p_i}; \mathbf{\Omega}_{uni}) - P(z_{p_j}; \mathbf{\Omega}_{uni})$ such that the steering control u_2 is [10]

$$u_2 = -K_p \Delta P_{ij}, \quad K_p > 0, \tag{16}$$

where i and j correspond to sensors placed on opposite sides of the body. Figure 5(a) shows three sensor pairing combinations used in the calibration process denoted by the blue pairing (z_{p_1}, z_{p_4}), the green pairing (z_{p_1}, z_{p_3}), and the red pairing (z_{p_2}, z_{p_3}). The corresponding pressure differences are plotted versus the angle of attack in Figure 5(b) for free stream flowspeed $U = 0.17$ m/s. The solid colored lines correspond to pressure differences based on potential flow theory, whereas the dashed lines correspond to experimental pressure differences. The shaded region of the experimental data curves correspond to one standard deviation of the measured differences. Note, due to flow separation and unmodeled viscous effects [10], the experimental pressure differences are less than the theoretically predicted differences at high angles of attack, resulting in larger angles of zero pressure difference for non-symmetric sensor pairs. The estimated flow speeds and analytically derived angles of zero pressure difference in Figure 5(b) provide flow conditions from which the procedure in equation (15) calculates the required IPMC calibration coefficients.

The bootstrapping procedure is as follows. The body is placed in an unknown uniform flow condition. The steering control (16) calculates the angular rate using pressure differences between a symmetric pair of pressure sensors. Choosing a symmetric pair steers the vehicle to zero angle of attack. Meanwhile, the recursive Bayesian filter assimilates distributed pressure difference measurements and produces an estimate of the free stream flowspeed. After sufficient settling time, we collect 500 samples from each IPMC sensor and compute the standard deviation from each sensor's samples.

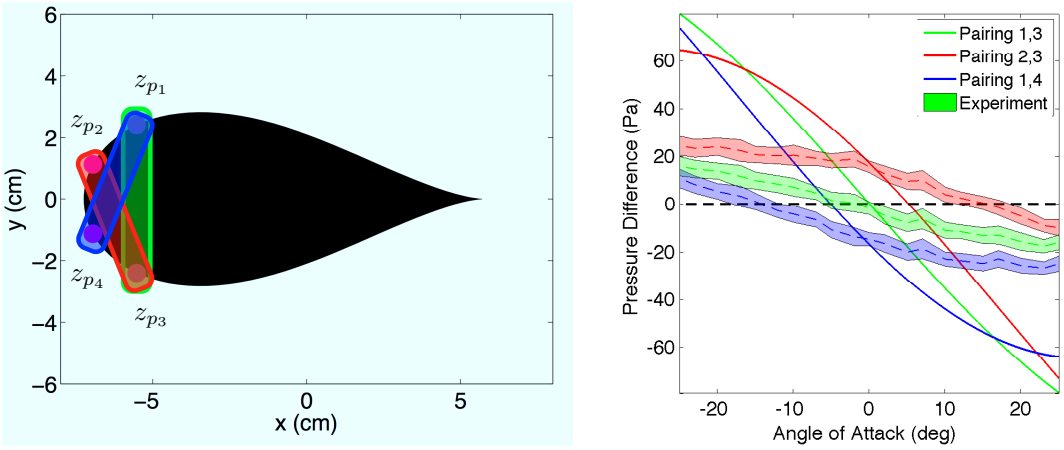

(a) (b)

Figure 5. (a) The position of sensors and sensor pair combinations used in the bootstrapping calibration procedure. (b) Experimental and theoretical pressure differences as a function of angle of attack for each pressure sensor pairing in (a). Shaded regions represent one standard deviation of the experimental measurements.

We record the estimated flowspeed, zero angle of attack, and standard deviation from each of the $N_f = 8$ IPMC sensors, which comprises sufficient data for all eight IPMC sensors at one flow condition combination in equation (15). Next, a pair of pressure sensors is chosen to stabilize a non-zero angle of attack, which we calculate analytically using the uniform potential flow model. After sufficient settling time we repeat the data collection and flowspeed estimation to produce an additional flow condition for equation (15). We repeat the process for all remaining non-symmetric sensor pairs for a given flowspeed, then change the free stream flowspeed and repeat the estimation and data collection procedure for all sensor pairs. The process produces a sufficient number of data points to calculate the optimal coefficients (a_k, b_k) in equation (15) for all $k = 1, \ldots, N_f$ IPMC sensors. This paper considers three pressure sensor pair combinations corresponding to the pressure sensors located on the surface of the foil with polar angles $(156.3°, -156.3°)$, $(170.7°, -156.3°)$, and $(156.3°, -170.7°)$ whose analytical zero pressure differences correspond to $0°$, $5.1°$, and $-5.1°$ angles of attack, respectively.

5. Experimental Results

This section presents experimental results generated using the hardware described in Section 4 and the estimation algorithms in Section 3. Sections 5.1 and 5.2 present experimental and numerical results for bio-inspired rheotaxis and station-holding, respectively.

A key benefit of the multi-sensor, multi-modal artificial lateral line presented in this work is its robustness to individual sensor or modal failure. Because of the distributed nature of the sensing array, failure of a single sensor will decrease estimation performance, but not inhibit operation. Likewise, loss of an entire sensing modality

(e.g., all eight IPMC sensors or all four pressure sensors) will not inhibit operation of the estimation scheme–though it would decrease performance. Moreover, the recursive Bayesian approach extends previous results [21], [22] by allowing non-symmetric and/or optimized sensor configurations and incorporating potential flow theory for model-based estimation as opposed to empirical or heuristic measurement models.

5.1. Experimental Demonstration of Rheotactic Control

This section uses the estimated flowfield parameters from the recursive Bayesian filter in a dynamic feedback controller that stabilizes the vehicle about a desired angle of attack α_{des}, which can have values other than zero. Rheotaxis corresponds to $\alpha_{des} = 0$, when the foil orients upstream. Assuming the motion of the body is governed by (5) and the cross-stream position is held fixed (i.e., $u_1 = 0$), we design the control $u_2 = u_2(\hat{\mathbf{\Omega}}_{uni})$ using feedback of the parameter estimates $\hat{\mathbf{\Omega}}_{uni} = (\hat{U}, \hat{\alpha})$ [31]. Suppose the estimated angle of attack can be modeled as $\hat{\alpha} = \alpha + \psi$, where the perturbation $|\psi| \leq \zeta$ is bounded [31]. Using a proportional control [31]

$$u_2(t) = K_\alpha(\alpha_{des} - \hat{\alpha}), \quad K > 0, \tag{17}$$

gives the closed-loop equation

$$\dot{\alpha} = K_\alpha(\alpha_{des} - (\alpha + \psi)). \tag{18}$$

The Lyapunov function $V = (\alpha - \alpha_{des})^2/2$ reveals that, if $\psi = 0$ and $\dot{\alpha}_{des} = 0$, then the quantity $\alpha - \alpha_{des} = 0$ is exponentially stable (see, e.g. [39, p. 114]). For $\psi \neq 0$, $\alpha(t)$ is uniformly, ultimately bounded for $|\psi| \leq \zeta$ with ultimate bound $|\alpha(t) - \alpha_{des}| \leq \zeta/K_\alpha$ [39, p. 347]. That is, by increasing K_α the steady-state error $\alpha - \alpha_{des}$ decreases.

We utilize the calibration procedure of Section 4.4 to represent each IPMC sensor measurement as a measurement of the square of the component of the flow normal to the sensor at each sensor location. Assimilating the IPMC flow measurements and pressure-difference measurements into the recursive Bayesian filter provides an estimate of the free stream flowspeed and angle of attack of the body over time. Experiments have shown that even after inhibiting measurements from either modality the estimation performance is still sufficient for performing rheotaxis.

The estimated angle of attack is used in the feedback control algorithm (17) to steer the vehicle toward a desired angle of attack. We assume pressure-difference and IPMC measurement variances of $\sigma_p^2 = 80$ Pa and $\sigma_{IPMC}^2 = 0.03$ m/s, respectively. The controller gain is $K = 0.2$ and the control and estimation loop runs at ~5 Hz.

Figure 6 illustrates experimental results of the flowfield estimation and control for rheotaxis under step inputs to the desired angle of attack. Figure 6(a) illustrates the marginal probability density‖ of the angle of attack estimation plotted versus time for a 75 second experiment. The color scale represents the one-dimensional probability density, where red areas represent larger probability density and blue areas denote the

‖ The marginal probability density is achieved by summing a multi-dimensional probability density over a subset of dimensions.

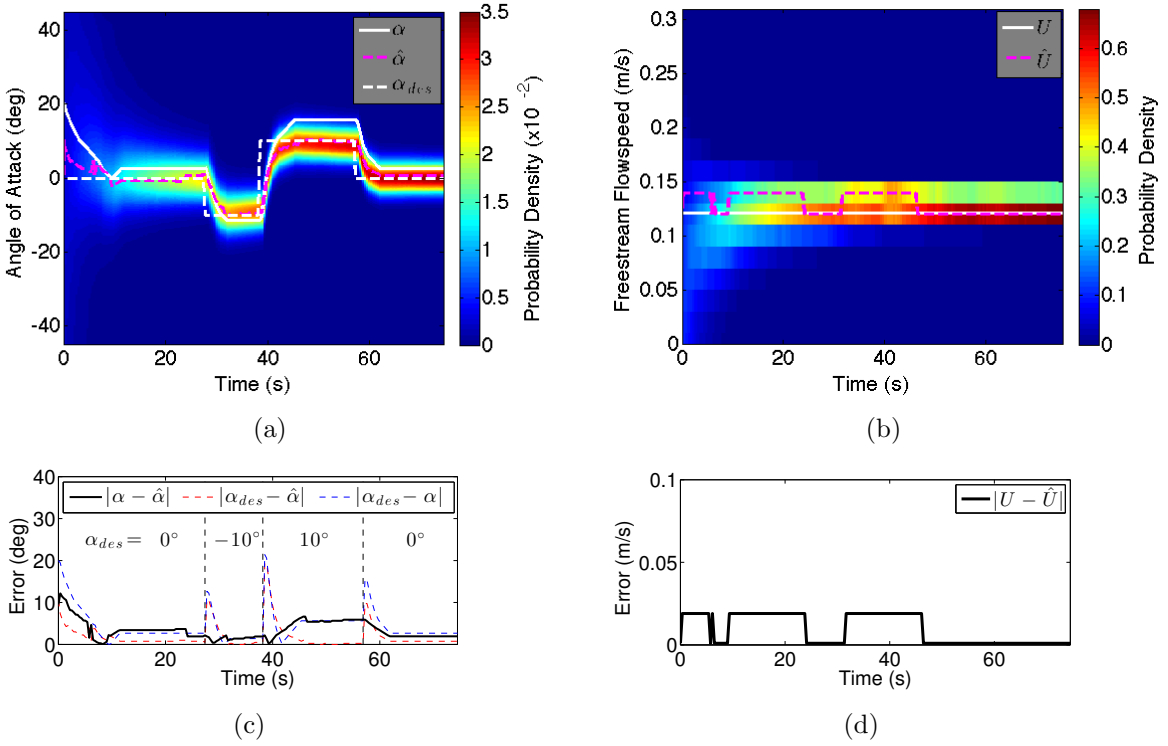

Figure 6. Experimental implementation of flow sensing and control for rheotaxis. (a) Marginal probability density of angle of attack plotted versus time with actual (solid white), estimated (dashed magenta), and desired (dashed white) angles of attack. (b) Marginal probability density of free stream flowspeed estimation plotted versus time with actual (solid white) and estimated (dashed magenta) free stream flowspeeds.(c) Absolute error between the desired, actual, and estimated angles of attack versus time. (d) Absolute error between the actual and estimated free stream flowspeed versus time.

opposite. The dashed white line corresponds to the desired angle of attack (α_{des}) versus time, whereas the magenta and solid white lines correspond to the estimated ($\hat{\alpha}$) and actual (α) angles of attack, respectively. Figure 6(b) shows the marginal probability density of the free stream flowspeed estimation versus time along with the actual (solid white) and estimated (dashed magenta) flowspeed. Note that as the recursive Bayesian filter converges to the actual angle of attack and flowspeed, the control algorithm steers the vehicle to the desired orientation, as illustrated by the distribution of probability density near the desired values.

Figures 6(c) and 6(d) illustrate the performance of the closed-loop system for regulation of angle of attack. Figure 6(c) shows the absolute error between the desired, estimated, and actual angles of attack versus time. The solid black line illustrates the absolute error between the actual and estimated angles of attack, whereas the dashed red and dashed blue lines denote the absolute error between the desired angle of attack and the estimated and actual angles of attack, respectively. The vertical dashed black lines denote the time instance when the desired angle of attack changes and the desired angle of attack is shown in each partitioned time frame. Note in Figure 6(c) that

after an initial transient phase the coupled estimation and control strategy maintains angle of attack error within five degrees, and within three degrees for the majority of the simulation. The largest error occurs after the transition from $\alpha_{des} = -10^\circ$ to $\alpha_{des} = 10^\circ$, which may be attributed to the model and calibration error discussed in Section 4.3. Note in Figure 6(d) that the free stream flowspeed estimation error remains within 0.02 m/s throughout the experiment.

5.2. Experimental Demonstration of Station-holding Control

This section presents experimental results of the station-holding control using the obstacle wake model (4). We implement a recursive Bayesian filter to estimate a subset of the obstacle flowfield parameters $\mathbf{\Omega}_{obs} = (y_{obs}, d)$, where y_{obs} is the cross-stream position and d is the diameter of the obstacle. The estimated cross-stream position is used to steer the vehicle behind the obstacle. The free stream flowspeed and upstream position of the obstacle are assumed to be known.

The flow conditions behind an obstacle at moderate to high Reynolds number are inherently unsteady and turbulent due to viscous effects, which are not modeled by potential flow theory. High-fidelity computational fluid dynamic models produce a more realistic representation of the fluid motion behind an obstacle, but require significant computation not suitable for real-time estimation. The model error introduced using potential flow may cause estimation error and even filter divergence. However, previous work has shown that potential flow theory captures the general time-average wake structure [23],[28],[29] of the wake, which is sufficient for estimating the cross-stream position of the obstacle given measurements from the multi-modal artificial lateral line and the spatial and temporal assimilation properties of the recursive filter. Here we use the potential flow model (4), extending previous potential flow modeling in [23], to include the presence of a foil and estimate the cross-stream position of the foil relative to the obstacle.

For station-holding control, let the angle of attack be held fixed (i.e., $\alpha = 0$, $u_2 = 0$) to facilitate design of the control $u_1 = u_1(\hat{\mathbf{\Omega}}_{obs})$ using feedback of the estimated cross-stream obstacle position $\hat{y}_{obs}$. Similar to the rheotactic control, suppose the estimated cross-stream position of the obstacle can be modeled as $\hat{y}_{obs} = y_{obs} + \psi$, where the perturbation $|\psi| \leq \zeta$ is bounded. We employ the proportional control

$$u_1(t) = K_s \hat{y}_{obs}, \quad K_s > 0, \tag{19}$$

giving the closed-loop equation for cross-stream obstacle position relative to the streamlined body (9),

$$\dot{y}_{obs} = -K_s(y_{obs} + \psi). \tag{20}$$

Lyapunov analysis shows that $y_{obs}(t)$ is exponentially stable for $\psi = 0$ and uniformly, ultimately bounded for $|\psi| \leq \zeta$ with bound $|y(t)| \leq \zeta/K_s$ [39, p. 347].

Figure 7 illustrates experimental results of the flowfield estimation and control algorithms for station-holding using the potential flow model (3) with velocity potential

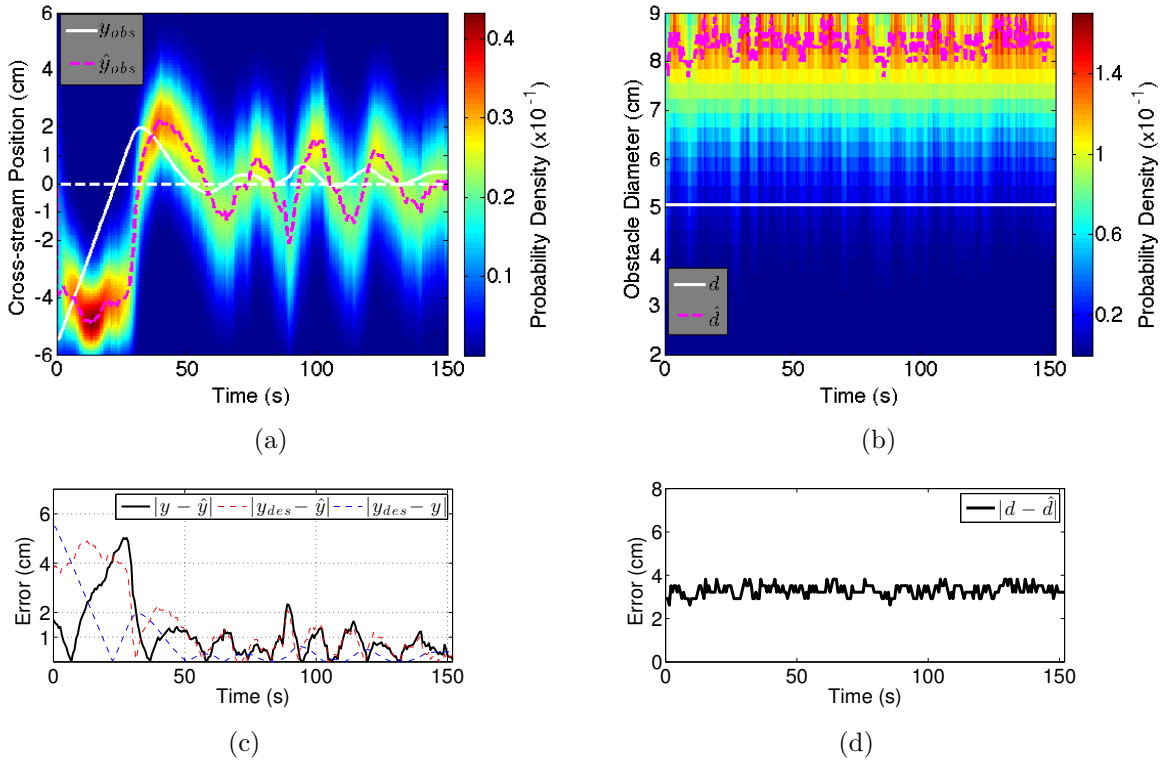

Figure 7. Experimental implementation of station-holding estimation and control. Marginal probability density of (a) cross-stream position and (b) obstacle diameter plotted versus time with actual (solid white) and estimated (dashed magenta) quantities. The dashed white line shows $y_{obs} = 0$ corresponding to when the foil lies directly behind the obstacle. (c) Absolute error between estimated, actual, and desired cross-stream positions and (d) actual and estimated obstacle diameter.

(4) and cross-stream control (19). An obstacle with diameter $d = 5.08$ cm was centered 5.08 cm upstream of the foil. To account for the significant model error, we assume measurement noise $\sigma_{f_k} = 0.1$ m/s and $\sigma_{p_j} = 80$ Pa for the calibrated IPMC and pressure-difference measurements, respectively. The free stream flowspeed is $U = 0.25$ m/s.

Figure 7(a) shows the marginal probability density of the estimated cross-stream position y_{obs}. The solid white line corresponds to the actual cross-stream position, whereas the dashed white and magenta lines correspond to the desired and estimated cross-stream positions, respectively. The initial cross-stream position was -5.5 cm. Figure 7(c) illustrates the absolute error between the actual and estimated cross-stream position (solid black) versus time as well as the absolute error between the desired cross-stream position and the estimated (dashed red) and actual (dashed blue) cross-stream positions. Note that despite the estimation error, the feedback control steers the foil to within 1 cm position error, as shown by the dashed blue line in Figure 7(c).

Figure 7(b) shows the marginal probability density of the estimated obstacle diameter. The estimated diameter is illustrated by the dashed magenta line, whereas the actual obstacle diameter is illustrated by the solid white line. Note that the recursive filter significantly overestimates the diameter of the obstacle. This error may

be attributed to unmodeled viscous and boundary layer effects that cause the wake of the obstacle to be larger than that predicted by potential flow theory. Measurements emulating a larger obstacle in the potential flow model affect the maximum likelihood estimate.

6. Conclusion

This paper describes the design and implementation of a multi-modal artificial lateral line for flow sensing and feedback control of an underwater vehicle. We use potential flow theory to model the flow around a foil in a uniform flow and in the presence of an upstream obstacle. Using the fluid model, we derive a measurement model consisting of local flow velocity and pressure-difference measurements inspired by the superficial and canal neuromasts of the fish lateral line. We design theoretically justified Bayesian filtering strategies based on the potential flow and measurement model to estimate properties of the flow for use in feedback control. A recursive Bayesian filter highlights the complementary nature of flow velocity and pressure difference measurements for estimating the flowspeed and angle of attack of a streamlined foil. In addition, we present a recursive Bayesian filter for estimating the cross-stream position of an obstacle in a moderate to high Reynolds number environment where the wake of the obstacle is turbulent. The estimated flow properties motivate the design of feedback control strategies to steer an underwater vehicle for bio-inspired behaviors including (positive) rheotaxis and station-holding. We steer the vehicle using proportional feedback control to a desired angle of attack or cross-stream position behind the obstacle.

This paper also presents the design and fabrication of an underwater robotic prototype outfitted with an artificial lateral line composed of eight IPMC flow sensors and four pressure sensors. We describe a novel bootstrapping methodology using pressure-difference measurements to calibrate the IPMC sensors for measuring flow velocity. Assimilating measurements from the calibrated artificial lateral line into an automatic control system that includes a two-degree-of-freedom gantry system experimentally demonstrates the rheotaxis and station-holding control and estimation algorithms in a flow channel.

The robustness of the control algorithm to estimation error is the subject of ongoing work. We also seek to adapt the experimental procedure and sensor configuration in order to detect the presence of vortices shed from an upstream obstacle at low Reynolds numbers. Current work employs dye-injection techniques to visualize the formation of shed vortices to better understand the sensor signature created on the artificial lateral line due to oncoming vortical structures. We also seek to derive flowfield estimation and control algorithms for high-fidelity flowfield and vehicle models, including models with coupled kinematics of the vehicle's angle of attack and cross-stream position. In addition, we continue to refine the fabrication and manufacturing process of the IPMC sensors in order to miniaturize each sensor while maintaining or improving the robustness of the array.

Acknowledgments

The authors of this work gratefully acknowledge Sheryl Coombs, Sean Humbert, Amanda Chicoli, and Badri Ranganathan for discussions related to this research. We also acknowledge James Tangorra and Jeffrey Kahn for discussions related to this work and for lending us pressure sensing equipment and Alison Flatau and Steve Day for lending us experimental equipment. We also acknowledge the anonymous reviewers whose constructive comments have significantly improved this work. This research is funded by the Office of Naval Research under Grant No. N00014–12–1–0149 and the 2013–2014 Link Foundation Ocean Engineering and Instrumentation Fellowship Program.

References

[1] S. Coombs, "Smart skins: Information processing by lateral line flow sensors," *Autonomous Robots*, vol. 11, no. 3, pp. 255–261, 2001.

[2] A. B. Kroese and N. A. Schellart, "Velocity and acceleration sensitive units in the trunk lateral line of the trout," *Journal of Neurophysiology*, vol. 68, pp. 2212–2221, 1992.

[3] S. Coombs and S. VanNetten, "The biomechanics and hydrodynamics of octavolateris sensory systems with special emphasis on the lateral line," in *Biomechanics (G. Lauder and R. Shadwick, eds). Fish Physiology.* Academic Press, 2006.

[4] C. F. Baker and J. C. Montgomery, "The sensory basis of rheotaxis in the blind Mexican cavefish, *Astyanax fasciatus*," *Journal of Comparative Physiology*, vol. 184, no. 5, pp. 519–527, 1999.

[5] B. L. Partridge and T. J. Pitcher, "The sensory basis of fish schools: Relative roles of lateral line and vision," *Journal of Comparative Physiology*, vol. 135, no. 4, pp. 315–325, 1980.

[6] M. McHenry, K. Feitl, J. Strother, and W. Van Trump, "Larval zebrafish rapidly sense the water flow of a predator's strike," *Biology Letters*, vol. 5, no. 4, pp. 477–479, 2009.

[7] H. Bleckmann, "Reaction time and stimulus frequency in prey localization in the surface-feeding fish *Aplocheilus lineatus*," *Journal of Comparative Physiology*, vol. 140, no. 2, pp. 163–172, 1980.

[8] A. M. Sutterlin and S. Waddy, "Possible role of the posterior lateral line in obstacle entrainment by brook trout (*Salvelinus fontinalis*)," *J. of the Fisheries Research Board of Canada*, vol. 32, no. 12, pp. 2441–2446, 1975.

[9] Z. Ren and K. Mohseni, "A model of the lateral line of fish for vortex sensing," *Bioinspiration & Biomimetics*, vol. 7, no. 3, May 2012.

[10] F. D. Lagor, L. DeVries, K. Waychoff, and D. A. Paley, "Bio-inspired flow sensing and control: Autonomous rheotaxis using distributed pressure measurements," *J. of Unmanned Systems Technologies*, vol. 1, no. 3, pp. 78–88, 2013.

[11] R. Venturelli, O. Akanyeti, F. Visentin, J. Jezov, C. L. D., G. Toming, J. Brown, M. Kruusmaa, W. M. Megill, and P. Fiorini, "Hydrodynamic pressure sensing with an artificial lateral line in steady and unsteady flows," *Bioinspiration & Biomimetics*, vol. 7, no. 3, Apr. 2012.

[12] Y. Yang, J. Chen, J. Engel, S. Pandya, N. Chen, C. Tucker, S. Coombs, D. L. Jones, and C. Liu, "Distant touch hydrodynamic imaging with an artificial lateral line," *Proceedings of the National Academy of Sciences*, vol. 103, no. 50, pp. 18 891–18 895, 2006.

[13] J. Tao and B. Yu, "Hair flow sensors: from bio-inspiration to bio-mimicking—a review," *Smart Materials and Structures*, vol. 21, no. 11, 2012.

[14] A. T. Abdulsadda and X. Tan, "Underwater tracking of a moving dipole source using an artificial lateral line: Algorithm and experimental validation with IPMC flow sensors," *Smart Materials and Structures*, vol. 22, p. 045010, 2013.

[15] A. Qualtieri, F. Rizzi, G. Epifani, A. Ernits, M. Kruusmaa, and M. De Vittorio, "Parylene-coated

bioinspired artificial hair cell for liquid flow sensing," *Microelectronic Engineering*, vol. 98, no. 0, pp. 516–519, 2012.

[16] V. I. Fernandez, A. Maertens, F. M. Yaul, J. Dahl, J. H. Lang, and M. S. Triantafyllou, "Lateral-line-inspired sensor arrays for navigation and object identification," *Marine Technology Society J.*, vol. 45, no. 4, pp. 130–146, 2011.

[17] Y. Yang, N. Nguyen, N. Chen, M. Lockwood, C. Tucker, H. Hu, H. Bleckmann, C. Liu, and D. L. Jones, "Artificial lateral line with biomimetic neuromasts to emulate fish sensing," *Bioinspiration & Biomimetics*, vol. 5, no. 1, 2010.

[18] A. Klein and H. Bleckmann, "Determination of object position, vortex shedding frequency and flow velocity using artificial lateral line canals," *Beilstein J. Nanotechnology*, vol. 2, pp. 276–283, June 2011.

[19] A. M. K. Dagamseh, T. S. J. Lammerink, M. L. Kolster, C. M. Bruinink, R. J. Wiegerink, and G. J. M. Krijnen, "Dipole-source localization using biomimetic flow-sensor arrays positioned as lateral-line system," *Sensors and Actuators*, vol. 162, no. 2, pp. 355–360, August 2010.

[20] A. Gao and M. Triantafyllou, "Bio-inspired pressure sensing for active yaw control of underwater vehicles," in *Oceans 2012*, Oct 2012, pp. 1–7.

[21] T. Salumae and M. Kruusmaa, "Against the flow: A Braitenberg controller for a fish robot," in *Proc. of the IEEE International Conference on Robotics and Automation*, 2012, pp. 4210–4215.

[22] ——, "Flow-relative control of an underwater robot," *Proc. of the Royal Soc. A*, vol. 469, no. 2153, March 2013.

[23] V. I. Fernandez, "Performance analysis for lateral-line-inspired sensor arrays," Ph.D. dissertation, Massachusetts Institute of Technology, June 2011.

[24] R. L. Panton, *Incompressible Flow*. John Wiley and Sons, 1984.

[25] L. Zhen, H. Beom-soo, K. Moo-rong, and J. Ji-yuan, "Experimental and numerical study for hydrodynamic characteristics of an oscillating hydrofoil," *J. of Hydrodynamics*, vol. 20, no. 3, pp. 280–287, 2008.

[26] J. D. Anderson, *Fundamentals of Aerodynamics*, 5th ed. McGraw-Hill, Feb. 2011.

[27] G. Birkhoff and E. H. Zarantonello, *Jets, Wakes and Cavities*. Academic Press, 1957.

[28] G. V. Parkinson and T. Jandali, "A wake source model for bluff body potential flow," *J. Fluid Mechanics*, vol. 40, no. 3, pp. 577–594, 1970.

[29] M. Kiya and M. Arie, "A free-streamline theory for bluff bodies attached to a plane wall," *J. Fluid Mechanics*, vol. 56, no. 2, pp. 201–219, 1972.

[30] L. M. Milne-Thomson, *Theoretical Aerodynamics*. Dover Publications, 1966.

[31] L. DeVries and D. A. Paley, "Observability-based optimization for flow sensing and control of an underwater vehicle in a uniform flowfield," in *Proc. of the 2013 Amer. Cont. Conf.*, Washington, DC, June 2013.

[32] N. Bergman, "Recursive Bayesian estimation navigation and tracking applications," Ph.D. dissertation, Department of Electrical Engineering, Linkoping University, Sweden, 1999.

[33] Y. Bar-Shalom, X. Rong Li, and T. Kirubarajan, *Estimation with Applications to Tracking and Navigation: Theory Algorithms and Software*, 1st ed. Wiley-Interscience, June 2001.

[34] Y. Bar-Cohen, *Electroactive Polymer Actuators as Artificial Muscles: Reality, Potential and Challenges*. Bellingham, WA: SPIE, 2001.

[35] M. Shahinpoor and K. J. Kim, "Ionic polymer-metal composites: I. Fundamentals," *Smart Materials and Structures*, vol. 10, no. 4, pp. 819–833, 2001.

[36] H. Lei, C. Lim, and X. Tan, "Modelling and inverse compensation of dynamics of base-excited ionic polymer-metal composite sensors," *J. of Intelligent Material Systems and Structures*, vol. 24, no. 13, pp. 1557–1571, 2013.

[37] A. Abdulsadda and X. Tan, "Nonlinear estimation-based dipole source localization for artificial lateral line systems," *Bioinspiration & Biomimetics*, vol. 8, no. 2, p. 026005 (15pg), Mar 2013.

[38] X. Chen, G. Zhu, X. Yang, D. L. Hung, and X. Tan, "Model-based estimation of flow characteristics using an ionic polymer-metal composite beam," *IEEE/ASME Trans. on Mechatronics*, vol. 18,

no. 3, pp. 932–943, June 2013.

[39] H. K. Khalil, *Nonlinear Systems*, 3rd ed. Prentice Hall, 2002.